electronics

MDPI

Article

Dynamic Imaging of Projected Electric Potentials of Operando Semiconductor Devices by Time-Resolved Electron Holography

Tolga Wagner [1,*,†], Hüseyin Çelik [2,†], Simon Gaebel [3], Dirk Berger [4], Peng-Han Lu [5], Ines Häusler [1], Nina Owschimikow [2], Michael Lehmann [2], Rafal E. Dunin-Borkowski [5], Christoph T. Koch [1] and Fariba Hatami [1]

1 Department of Physics, Humboldt-Universität zu Berlin, Newtonstraße 15, 12489 Berlin, Germany; ines.haeusler@physik.hu-berlin.de (I.H.); christoph.koch@hu-berlin.de (C.T.K.); hatami@physik.hu-berlin.de (F.H.)
2 Institute of Optics and Atomic Physics, Technische Universität Berlin, Straße des 17. Juni 135, 10623 Berlin, Germany; celik@tu-berlin.de (H.Ç.); nina.owschimikow@physik.tu-berlin.de (N.O.); michael.lehmann@tu-berlin.de (M.L.)
3 Max-Born-Institut, Max-Born-Straße 2A, 12489 Berlin, Germany; simon.gaebel@mbi-berlin.de
4 Center for Electron Microscopy ZELMI, Technische Universität Berlin, Straße des 17. Juni 135, 10623 Berlin, Germany; dirk.berger@tu-berlin.de
5 Ernst Ruska-Centre for Microscopy and Spectroscopy with Electrons, Forschungszentrum Jülich, 52425 Jülich, Germany; p.lu@fz-juelich.de (P.-H.L.); r.dunin-borkowski@fz-juelich.de (R.E.D.-B.)
* Correspondence: tolga.wagner@physik.hu-berlin.de
† These authors contributed equally to this work.

Abstract: Interference gating (iGate) has emerged as a groundbreaking technique for ultrafast time-resolved electron holography in transmission electron microscopy, delivering nanometer spatial and nanosecond temporal resolution with minimal technological overhead. This study employs iGate to dynamically observe the local projected electric potential within the space-charge region of a contacted transmission electron microscopy (TEM) lamella manufactured from a silicon diode during switching between unbiased and reverse-biased conditions, achieving a temporal resolution of 25 ns at a repetition rate of 3 MHz. By synchronizing the holographic acquisition with the applied voltage, this approach enables the direct visualization of time-dependent potential distributions with high precision. Complementary static and dynamic experiments reveal a remarkable correspondence between modeled and measured projected potentials, validating the method's robustness. The observed dynamic phase progressions resolve and allow one to differentiate between localized switching dynamics and preparation-induced effects, such as charge recombination near the sample edges. These results establish iGate as a transformative tool for operando investigations of semiconductor devices, paving the way for advancing the nanoscale imaging of high-speed electronic processes.

Keywords: ultrafast electron holography; transmission electron microscopy; nanostructured device; semiconductor electronics; dynamic imaging

check for updates

Academic Editor: Fei Song

Received: 29 November 2024
Revised: 2 January 2025
Accepted: 3 January 2025
Published: 5 January 2025

Citation: Wagner, T.; Çelik, H.; Gaebel, S.; Berger, D.; Lu, P.-H.; Häusler, I.; Owschimikow, N.; Lehmann, M.; Dunin-Borkowski, R.E.; Koch, C.T.; et al. Dynamic Imaging of Projected Electric Potentials of Operando Semiconductor Devices by Time-Resolved Electron Holography. *Electronics* **2025**, *14*, 199. https://doi.org/10.3390/electronics14010199

1. Introduction

As electronic devices continue to shrink in size [1–10], their performance is increasingly governed by nanoscale phenomena, where surface effects, charge dynamics, and localized interactions play a pivotal role [11–14]. Modeling and optimizing these devices require simulations capable of resolving dynamic processes at ultrafast timescales. However, conventional modeling [15–19] and experimental techniques [20–23] often fall short in capturing localized transient effects, particularly in active regions where ultrafast switching and charge transport mechanisms are critical. From an experimental standpoint, due to structural dimensions, the use of electron microscopic techniques is unavoidable for quantitative investigations of the general behavior of real-world nano-devices.

Transmission electron microscopy (TEM) has evolved over its 90-year history into one of the most powerful tools for the quantitative analysis of materials, offering spatial resolution down to the atomic scale [24]. Off-axis electron holography (EH), an advanced TEM technique, goes a step further by providing access to the amplitude and phase of reconstructed electron waves [25]. The reconstructed phases, in particular, encode spatially resolved information about projected electromagnetic potentials [26,27], making EH an excellent tool for studying electric potential distributions in semiconductor devices [28]. When combined with in situ specimen holders that allow devices to be operated during investigations, EH offers unique insights into the internal mechanisms of these devices [29–34].

Despite these capabilities, existing methods for time-resolved measurements in a TEM, primarily based on pulsed photoemission, have proven incompatible with EH [35,36], limiting electron holographic investigations to static states. Consequently, the dynamic switching processes in semiconductor nano-devices have remain unexplored using electron holographic techniques. This gap highlights the pressing need for dynamic imaging methods capable of capturing nanoscale electric potential distributions under operando conditions with ultrafast temporal resolution.

In this context, interference gating (iGate) [37,38] has emerged as a transformative technique for ultrafast time-resolved electron holography, addressing many of the aforementioned limitations. By synchronizing holographic acquisitions with fast electronic processes, iGate enables the direct visualization of time-dependent distributions of projected potentials at nanometer spatial and nanosecond temporal resolution. This capability bridges the longstanding gap between static and dynamic investigations, offering a unique view into transient behaviors such as charge transport, electric field evolution, and switching dynamics in semiconductor devices. The integration of iGate into in situ TEM-based EH thus opens a new frontier for operando imaging, paving the way for a deeper understanding of ultrafast electronic processes at the nanoscale.

In this study, the capabilities of iGate are demonstrated through a proof-of-concept experiment. Specifically, the localized temporal progressions of the projected microscopic electric potential of a contacted TEM lamella, prepared out of a commercial macroscopic fast-switching silicon diode [39], are investigated with a temporal resolution of 25 ns at a repetition rate of 3 MHz. The results establish iGate as a robust spatio-temporal measurement technique for probing locally dependent dynamic effects in semiconductor devices, while also confirming its applicability for investigating the nanoscopic potential dynamics of nanostructured devices, provided that the remaining challenges are addressed. Furthermore, an analysis of these challenges is presented, along with perspectives on strategies to overcome them.

2. Methods

This section provides the theoretical and practical foundations of the methodologies, detailing the experimental setup, data acquisition, sample preparation, and modeling approach.

2.1. Operando Off-Axis Electron Holography

In the past decades, off-axis electron holography has emerged as a widely used phase-resolving measurement technique in electron microscopy. For a complete picture of this method, readers are referred to the following review articles and textbooks: [27,40–42]. The following section serves more as a brief overview of the core concepts behind EH and a description of the instrumentation needed for operando investigations.

As a two-step process, consisting of the acquisition of the electron hologram (Figure 1a) and its subsequent reconstruction (Figure 1b), EH's strength lies in its ability to image both the amplitude and the phase modulation of an electron wave passing through a sample. The approach, pioneered by Möllenstedt and Düker in the 1950s [43], utilizes an electron optical biprism, located near the selected area aperture plane (Figure 1a), to overlap two partial electron waves, neglecting aberrations of the objective lens: an object wave (Obj),

$$\psi_{obj}(\vec{r}) = a_{obj}(\vec{r})e^{i\varphi_{obj}(\vec{r})}, \quad (1)$$

that has passed through the sample and a reference wave (Ref),

$$\psi_{ref}(\vec{r}) = a_{ref}(\vec{r})e^{i\varphi_{ref}(\vec{r})}, \quad (2)$$

that passes through a nearby vacuum region, where $\vec{r} = (x, y)$ describes 2D coordinates, $a_{obj}(\vec{r})$ and $a_{ref}(\vec{r})$ are the amplitudes, and $\varphi_{obj}(\vec{r})$ and $\varphi_{ref}(\vec{r})$ are the phases of both partial waves, respectively. At this point, it should be noted that the reference wave is not generally to be regarded as unmodulated and the reconstructed phase, therefore, does not necessarily represent the phase modulation of the object wave. This is particularly true for electrically biased samples, which may feature strong stray fields. This represents a well-known problem, the so-called perturbed reference wave (PRW) [44–46].

The overlap leads to a superposition of both partial waves and, hence, to the formation of an interference pattern, the electron hologram:

$$I_{hol}(\vec{r}) = a_{obj}(\vec{r})^2 + a_{ref}(\vec{r})^2 + 2\mu a_{obj}(\vec{r})a_{ref}(\vec{r})\cos(2\pi\vec{q}\cdot\vec{r} + \underbrace{(\varphi_{obj}(\vec{r}) - \varphi_{ref}(\vec{r}))}_{\varphi(\vec{r})}), \quad (3)$$

in the detector plane over an exposure time T_{exp}, where $\vec{q}$, with its magnitude $|\vec{q}| = s^{-1}$ being inverse proportional to the fringe spacing s, represents the spatial carrier frequency determined by the overlap angle β, $\varphi(\vec{r})$ is the phase difference between the object and reference waves, representing the phase of the reconstructed electron wave $\psi(\vec{r})$ (Figure 1b, last panel), and μ represents the fringe contrast or fringe visibility V_{hol} defined by Michelson [47].

After acquiring the hologram, the complex electron wave $\psi(\vec{r})$ can be reconstructed through a series of Fourier operations (Figure 1b). In Fourier space, the hologram yields a centerband containing (ideally) only amplitude information and two sidebands containing amplitude and phase information. Selecting and inverse-transforming only "one" sideband, by means of a circular mask with a cut-off frequency f_{cut} as its radius in Fourier space, enables the retrieval of both the amplitude and the phase image $\varphi(\vec{r})$, which provides access to the sample's internal electromagnetic potentials.

In the absence of a magnetic potential, the phase shift $\varphi_{obj}(\vec{r})$ caused by an electric potential $V(\vec{r}, z)$ within and surrounding the sample is given by

$$\varphi_{obj}(\vec{r}) = \frac{\pi}{\lambda E}\int V(\vec{r}, z)\,dz = \frac{\pi}{\lambda E}V_{proj}(\vec{r}), \quad (4)$$

where λ is the electron wavelength, E is the relativistic electron energy, and $V(\vec{r})$ is the potential along the electron's path through the sample. This phase shift directly maps the projected potential $V_{proj}(\vec{r})$, making off-axis holography a valuable tool for studying electrical properties in semiconductor devices down to the nanoscale.

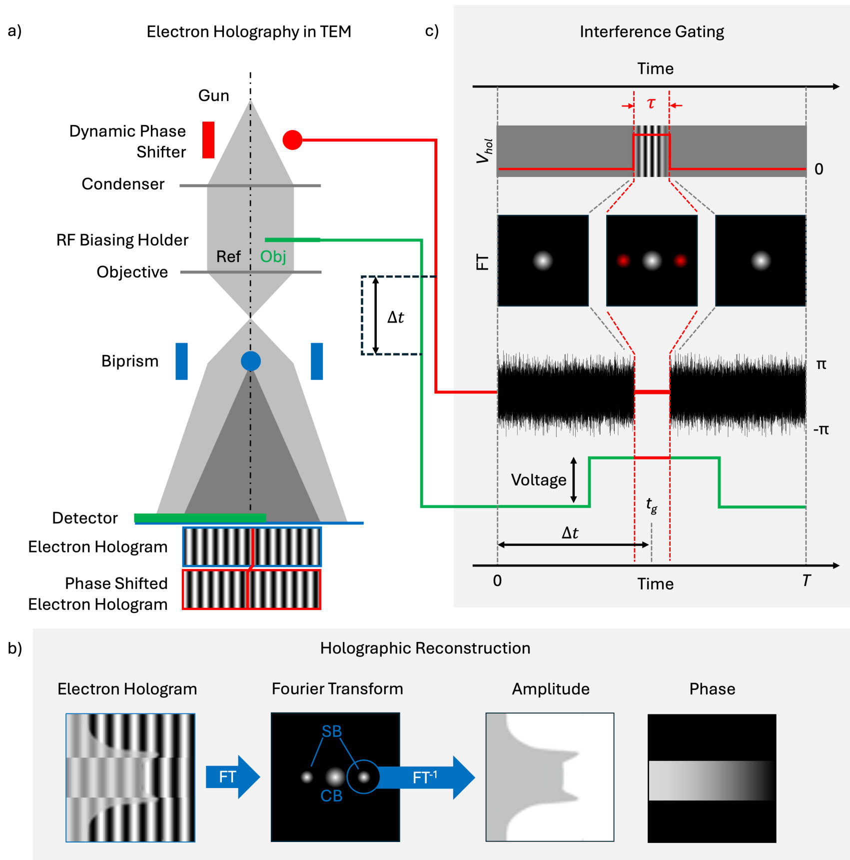

Figure 1. Schematic of the time-resolved electron holography setup with interference gating in a transmission electron microscope (TEM). (**a**) The TEM configuration uses an RF biasing holder to apply a periodic voltage to the sample, creating an electron hologram by overlapping object (Obj) and reference (Ref) waves with a biprism. (**b**) Holographic reconstruction process: Fourier transformation (FT), isolating sideband (SB) from centerband (CB), extracting amplitude and phase information. (**c**) Interference Gating: dynamic fringe contrast V_{hol} with gate length τ (top panel), FT within and outside the gate (second panel), noise-based gating signal applied to dynamic phase shifter (third panel), control signal applied to RF biasing holder (bottom panel), synchronized to each other with an adjustable temporal delay Δt for setting the gate position t_g.

The following electron holographic experiments feature two different setups:

1. Electron holograms from static experiments with a large field of view (FoV) that extends over the entire object under investigation (approx. 23.4 µm × 24.6 µm) were acquired on the FEI Titan G^2 60-300 Holo in Jülich, Germany [48]. For this purpose, a special low-mag mode was used at an acceleration voltage of $U_{acc} = 300$ kV, in which neither the objective lens nor the conventional Lorentz lens is used for imaging. Ten electron holograms with an exposure time of $T_{exp} = 1$ s each were acquired by a Gatan K2 direct electron detector. The holograms feature a fringe spacing of $s = 40$ nm over a hologram width of $w_{hol} = 19$ µm and are averaged using the HoloWorks 6 plugin [49] for DigitalMicrograph 3 [50] during the reconstruction, with a cut-off frequency of $f_{cut} = 8\,\mu m^{-1}$;
2. Time-resolved electron holograms were acquired on the FEI Titan 80-300 Holography Special Berlin TEM [51] in Berlin, Germany at an acceleration voltage of $U_{acc} = 200$ kV in a special extended Lorentz microscopy mode (detailed description given in [38]) with a smaller field of view (approx. 5.3 µm × 5.3 µm) that captures a more central region in the object under investigation. This setup also features an additional decentered biprism in the C2 aperture plane condenser system, acting as a dynamic

phase shifter (Figure 1b), capable of introducing slight tilts in the electron beam at radio frequencies (RF). At each gate position t_g, five time-resolved electron holograms with an exposure time of $T_{exp} = 8\,\text{s}$ each were acquired by a Gatan US1000 CCD detector. These holograms feature a fringe spacing of $s = 25\,\text{nm}$ over a hologram width of $w_{hol} = 6\,\mu\text{m}$ and are averaged using the holoaverage software package [37] during the reconstruction with a spatial cut-off frequency in Fourier space of $f_{cut} = 11\,\mu\text{m}^{-1}$.

Furthermore, all holograms were normalized during the reconstruction by unbiased ones (i.e., $U_{ext} = 0\,\text{V}$), leading to reconstructed phases that only show the modulation induced by an external bias as features like inherent potentials, while modulations due to artifacts (e.g., dynamic diffraction) are compensated. In both setups, a modified Protochips Aduro Specimen Holder served as an RF biasing holder, enabling the static electrical biasing and rapid switching of the sample for operando investigations. Constant voltages for static biasing experiments were applied using a Keithley 2450 source meter, while the dynamic signals for the time-resolved experiments were generated and synchronously applied by a GW Instek MFG-2260MRA arbitrary waveform generator (both from the same laboratory in Berlin, Germany). The parameters for the gating signal were chosen such that the amplitude of the noise (without gate) with $U_G \approx 2.7\,\text{V}$ ensures that the interference pattern is completely canceled out.

2.2. Time-Resolved Electron Holography by Interference Gating

In recent years, interference gating (iGate) has emerged as a promising and robust method for acquiring time-resolved electron holograms. A detailed description of the method and its implementation in TEM can be found in [37,38,52]. In the following, a brief description of its basic idea and mechanics is given with reference to Figure 1c.

The method is based on the intentional destruction of the interference pattern for a large part of a measurement, utilizing short undisturbed time periods (called gates), which are synchronized to a periodic process under investigation, to generate time-resolved interferometric information. Thereby, iGate represents a fundamentally novel shutter mechanism for the generation of time-resolved information, which is neither based on a total suppression of the amplitude (i.e., conventional mechanical shutter or stroboscopic illumination) nor on an artificial temporal segmentation (readout time) of the intensity (i.e., ultrafast detection). In comparison, the presented method uses only a dynamic phase shift between two partial waves for a synchronized suppression or enabling of the formation of an interference pattern. In particular, its simple technical realization (i.e., only a two-channel signal generator and two coaxial cables) enables low-barrier access to the investigation of ultrashort periodic phenomena on existing instruments.

Figure 1c conceptually illustrates iGate, which enables time-resolved electron holography by selectively synchronizing the formation of an interference pattern (top panel) with a periodic external voltage signal (green curve, bottom panel). The panels, from top to bottom, show the visibility V_{hol} of the interference fringes (red curve) according to Equation (3), the Fourier transforms of disturbed electron holograms outside and undisturbed ones within the gate (second panel), and the correlated periodic gating signal (black and red curve, third panel) applied to the dynamic phase shifter.

In the top panel, the visibility of the interference fringes is depicted as an interference pattern in the background. These fringes, which are essential for capturing phase information, appear only during the selected gating intervals τ when the interference pattern is allowed to form. Outside these intervals, the interference pattern is intentionally disrupted, eliminating fringe visibility V_{hol}. This selective gating creates brief periods where the acquisition of interferometric information is switched “on”, shown by visible fringes, allowing phase information to be acquired at specific time points (or gate positions t_g) within each cycle.

The second panel shows exemplary Fourier transforms outside, featuring only center band (CB) information, and inside, featuring additional sidebands (SB), the gate. The latter carry the desired amplitude and phase information. Since the acquisition over the exposure time T_{exp} is an integrative process, the time-resolved hologram contains the sum of all time points (with and without SBs), where the holographic reconstruction acts as a temporal filter, which only encodes the interferometric information from the gate τ. iGate is thus independent of the readout time of the detector used.

For the technical implementation, a noise-based gating signal (black and red curve, third panel) is applied to the dynamic phase shifter, synchronized to the control signal applied to the sample (green curve, bottom panel). The latter varies over a period T and hence induces potential changes in the sample. The gating intervals τ, marked in red, are aligned with specific time points in the period T (gate position t_g) that can be shifted by Δt relative to the control signal (green curve, bottom panel) in order to sample the whole periodic process. By this, iGate provides temporal snapshots of the sample's potential distribution.

2.3. Preparation of Contacted TEM Lamella

The objective of this experiment is to evaluate the potential of interference gating for investigating electric nano-devices by applying it to a conventional semiconductor component, namely, an ultrafast switching silicon diode (UG1A [39]). This serves as a proof-of-concept to determine whether time-resolved electron holography (EH)—specifically, iGate—can effectively capture dynamic processes in such devices. A key challenge for this is the preparation of a suitable sample, which involves creating a contacted, electron-transparent TEM lamella. While a detailed explanation of the complete preparation process and the electrical characterization of the diode is provided in [52,53], this section concentrates on summarizing the most critical steps. Using Figure 2a, an overview of the sample structure and the experimental setup is presented to ensure the clarity and understanding of the procedure.

The UG1A diode, manufactured using thermal diffusion for doping the Boron-doped silicon waver with phosphorus, is expected to have an extended space-charge region (SCR) that spans several µm. The preparation for this diode involves a series of precise steps, beginning with mechanical preparation to create a suitable sample for further focused ion beam (FIB) processing. Initially, the whole device is mechanically ground (utilizing a T-tool grinding device [54]) in order to reduce its overall size and achieve a polished surface. By this, the p- and n-contacts with the device situated centrally between them are exposed (macroscopic view in the first panel of Figure 2a).

After this, the exact position of the p-n junction is determined through voltage contrast microscopy in a scanning electron microscope (SEM). By applying a reverse bias of $U_{ext} = -2\,\text{V}$ across the contacts using the micro-manipulator (transfer needle), a potential difference becomes visible across the diode, with a strong contrast near the p-contact. This contrast, highlighted in the second panel of Figure 2a, identifies the p-n interface, enabling accurate targeting during FIB preparation.

For the FIB preparation, an FEI Helios NanoLab 600 located in Berlin, Germany with 30 kV Ga-ion beams of 2.8 nA, 280 pA, and 93 pA was used for the extraction, thinning, and polishing of the lamella. The final sample, shown in the third and fourth panels of Figure 2a, is an electron-transparent foil, approx. 22 µm in length, 8 µm in width, and 400 nm in thickness, contacted on an FIB-optimized carrier chip (Protochips) using FIB-deposited Pt. This special configuration, in which the p–n interface lies parallel to the contacts of the carrier chip, allows for the application of a controlled electrical bias across the diode in the TEM while minimizing the probability of a short circuit.

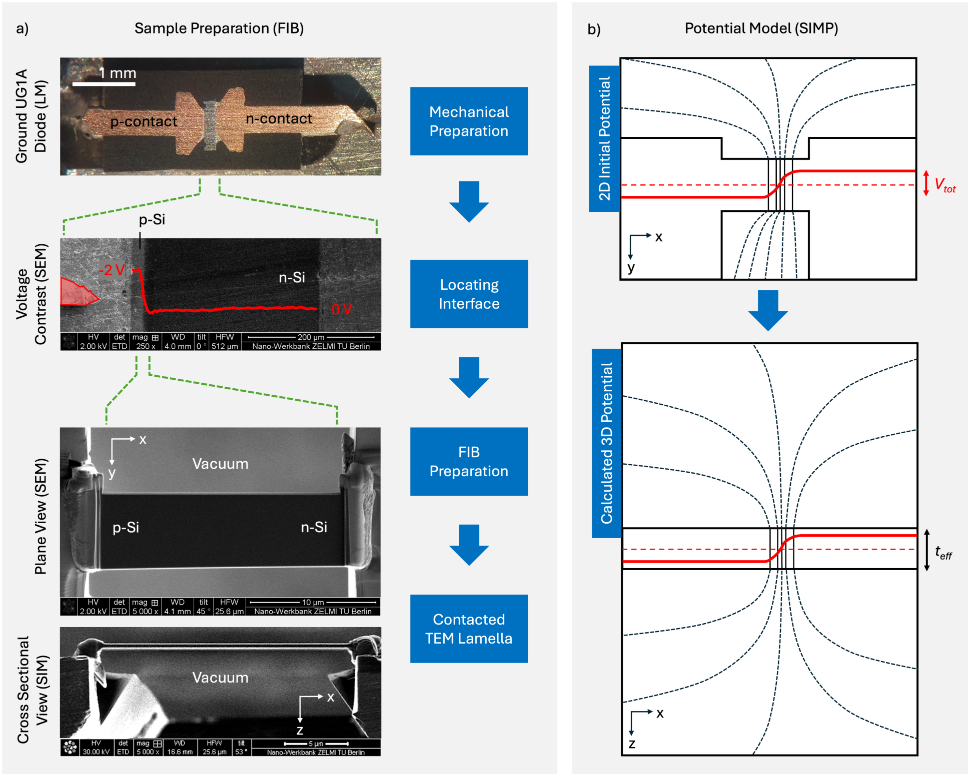

Figure 2. (**a**) Sample preparation and multiscale imaging of the UG1A diode, showcasing the individual steps, ranging from the mechanical preparation to the contacted TEM lamella. The top panel shows a macroscopic view (light microscopy, LM) of the mechanically ground UG1A diode with the device visible, centered in between p- and n-contacts. The middle panel displays a voltage contrast image acquired by Scanning Electron Microscopy (SEM) utilizing a micro-manipulator (colored red) as an electrical contact, indicating a potential difference across the p–n junction interface (plotted in red, from -2 V on the p-side to 0 V on the n-side). The bottom panels show SEM images of the FIB-prepared lamella in top (electron image) and side views (ion image), highlighting the p- and n-doped areas within and the vacuum region surrounding the sample. (**b**) Potential model using SIMP. The upper diagram depicts the initial 2D potential distribution across the p–n junction (red line) and within the supporting chip with an applied reverse-bias V_{tot}, while the black dashed lines represent the electric potential extending into the vacuum calculated by SIMP. The lower diagram shows a schematic cross-section of the SIMP-based extension of the initial 2D potential with an effective thickness t_{eff} along the z-axis to the full 3D potential distribution, needed for calculating the projected potentials and simulated phases.

2.4. Modeling of Projected Potentials

Accurately modeling the electrostatic potential distribution of semiconductor devices, such as the UG1A diode, is essential for understanding device behavior but is often computationally demanding. The Simple and Intuitive Model for Potentials (SIMP) addresses this by modeling the potential distribution through a diffusion equation, where the solution is a heat kernel that naturally adopts a Gaussian shape across all dimensions [55]. Through independent convolutions of the initial potential distribution with a propagation-distance-dependent Gaussian kernel, SIMP efficiently captures the potential spread into the surrounding vacuum with minimal computational load.

In detail, SIMP can first be utilized to construct the 2D initial potential distribution of the UG1A diode in the x–y-plane (Figure 2b, upper diagram), where the 1D initial potential distribution inside the device is determined using the analytical p–n junction equation (Figure 2b, red curve in the upper diagram) for any arbitrary externally applied reverse bias V_{tot} [56]. In obtaining this 1D initial potential distribution, the SCR is set to 4.5 µm in width. The potential at the supporting chip is held at a constant value of $\pm V_{tot}/2$, and the modeled area spans 45 µm × 89 µm. Additionally, boundary conditions at the lower edge of the modeled x–y plane impose a potential with a linear gradient profile in the x-direction in between the two sides of the supporting chip. Using the same approach of independent convolutions, the 3D potential distribution is subsequently calculated by applying a normalized, propagation-distance-dependent Gaussian kernel (Figure 2b, lower diagram). This yields a total 3D volume that spans 45 µm × 89 µm × 40 µm, with a sampling factor of 1 px ≅ 10 nm in all dimensions, resulting in a total number of 160,200,000,000 nodes. To obtain the modeled phase shift, this 3D potential distribution is then projected along the z-axis according to Equation (4), where t_{eff} describes the effective thickness (and its contribution) to the overall phase shift. In order to obtain comparable phase images to the experimental measurement conditions, an object and reference wave region can likewise be defined and subtracted from each other, satisfying Equation (3). Additionally, the projected potential of the unbiased diode (built-in potential) is subtracted from all projections with different applied voltages to account for the normalization in the experiments. Furthermore, a half-modeling approach that utilities the axial symmetry of the sample around the z-axis can be used to reduce the computational complexity of the calculations. For the geometry described above, the total computation time on an Intel i9-14900KF CPU is less than 5 min.

3. Experimental Results and Discussion

In the following, the experimental results are described in the context of comparisons between modeled and measured static phases as well as the transition to the dynamic phases. The aim is to correlate the reduced fields of view from the time-dependent measurements with the projected potential distribution of the entire device.

3.1. Static Imaging of Projected Potentials

An important step in the analysis of reconstructed phases of measurements with large fields of view is the comparison with suitable models of the sample. The reason for this is the non-negligible influence of electrical stray fields on the reference wave, especially in operando experiments with electronic devices. Figure 3a shows the calculated normalized phase (according to Equation (4)) from the projected 3D potential (SIMP). In the area of the diode (indicated by the dashed white rectangle centered in the object wave region, lower white rectangle), a monotonic increase from the p- to the n-side can be clearly observed. However, if the phase from the reference wave region (upper white rectangle) is subtracted (Equation (3)), this results in a strongly deviating phase course (Figure 3b, top row). Here, especially for the reverse-biased diode (dashed white rectangle), a phase valley can be observed in the region of the p-doped side. At this point it should be noted that this is only caused by the perturbed reference wave and is not related to a possible potential well within this region. Overall, for the modeled normalized phases in the upper row, it can be observed that the total phase shift drops linearly with decreasing reverse bias. For the unbiased diode, the normalization (subtraction of the 0 V phase) results in a constant modeled phase course.

A similar pattern emerges for the reconstructed phases from the static electron holographic measurements with large FoV (Figure 3b, bottom row) at all three applied voltages of $U_{ext} = -2$ V, -1 V, and 0 V. In addition to a strong visual similarity between modeled and experimental phases, especially with regard to the phase valley in the p-doped region of the diode, the plotted phases for all voltages in Figure 3c (taken from the lower region of the diode, indicated by the white arrow) show an excellent agreement in their courses. Only in the vicinity of $x = 8\,\mu m$ are there small deviations, which can be attributed to dynamic electron diffraction due to the bending of the TEM lamella. Considering the simplicity of the model, the agreement of the phase courses for the reverse-biased cases is remarkable. Only for the unbiased case is there a deviation towards the contacts (especially towards the p-contact). Possible causes for this may include surface effects (e.g., charging) or potential barriers at interfaces (i.e., Schottky barrier), which are not taken into account in the model. However, since this effect is not observed in the biased cases, it is highly likely caused by accumulated charges on the surface and at the interface.

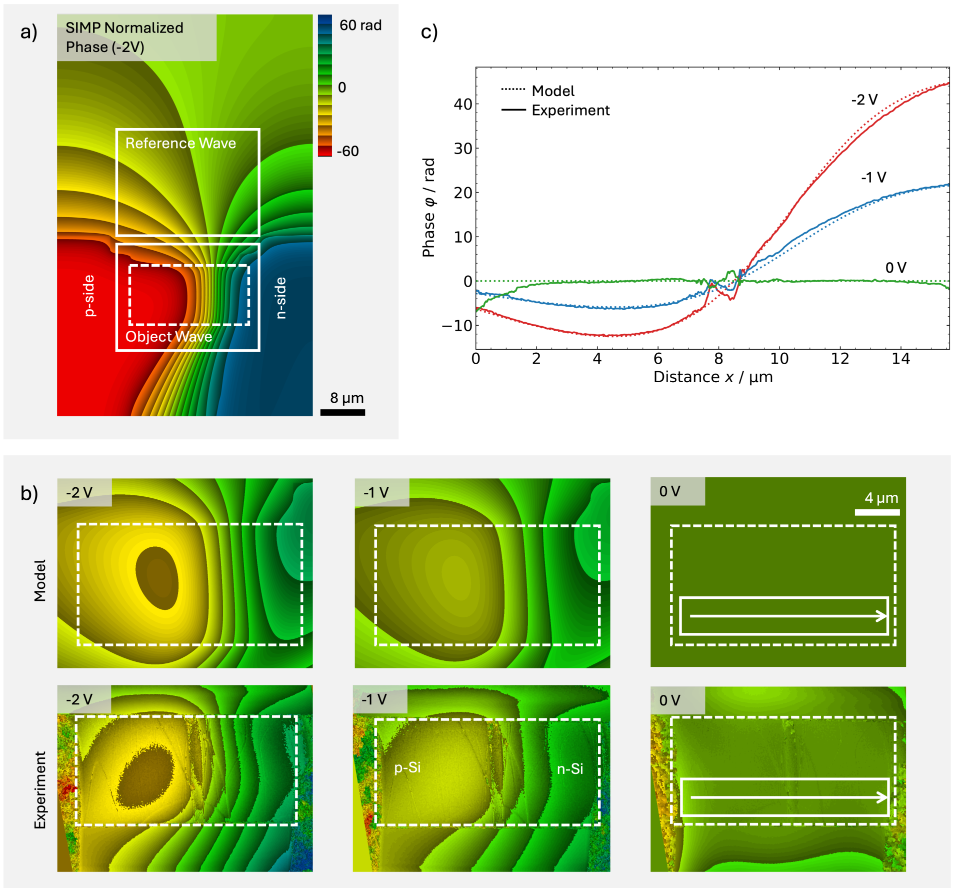

Figure 3. (**a**) Normalized simulated phase (calculated by SIMP) of the UG1A diode under reverse-bias condition ($U_{ext} = -2\,V$). The white boxes indicate the areas used as reference and object wave regions in the static electron holographic experiments and the dashed white box highlight the area of the contacted TEM lamella. (**b**) Comparison of the modeled phase (difference between object and reference wave regions, top row) with experimental phase reconstructions (bottom row) at different applied biases: $U_{ext} = -2\,V$, $-1\,V$, and $0\,V$. The dashed white boxes highlight the area of the contacted TEM lamella. (**c**) Phase profiles extracted from SIMP (dotted lines) and experimental data (solid lines) across the diode for varying biasing conditions.

3.2. Dynamic Imaging of Projected Potentials

For the transition to dynamic imaging, Figure 4 is used to discuss the comparability to the static measurements, in particular taking into account the strongly differing fields of view between static and dynamic measurements. As an overview, the reconstructed phase for $-1\,V$ from Figure 3b, bottom row, is shown in Figure 4a. Here, the field of view for the time-resolved measurements is additionally marked with an orange polygon. Corresponding reconstructed dynamic phases are shown in Figure 4b. These originate from a time-resolved experiment in which the diode is operated with a square-wave signal that switches between unbiased (i.e., $U_{ext} = 0\,\text{V}$) and reverse-biased conditions (i.e., $U_{ext} = -1\,\text{V}$) at a repetition rate of $f = 3\,\text{MHz}$, resulting in a period of $T = 333.3\,\text{ns}$. The dynamic phases were reconstructed from time-resolved electron holograms recorded using iGate, whereby the noise-based gating signal has a peak-to-peak amplitude of 2.7 V, a gate length of $\tau = 25\,\text{ns}$, and a sampling resolution (i.e., temporal distance between gate positions) of $\Delta t = 11.1\,\text{ns}$. The phases shown correspond to gate positions at $t = 150\,\text{ns}$ and $t = 61\,\text{ns}$, which correlate with reverse-biased and unbiased conditions, respectively. Analogous to the static measurements, the areas and directions from which the phase profiles (Figure 4c–e) were taken are marked in orange. Visually, the reverse-biased phases from the static and dynamic experiments, despite strongly differing fields of view, appear to match very well. A more detailed insight can be obtained by comparing the phase profiles plotted in Figure 4c.

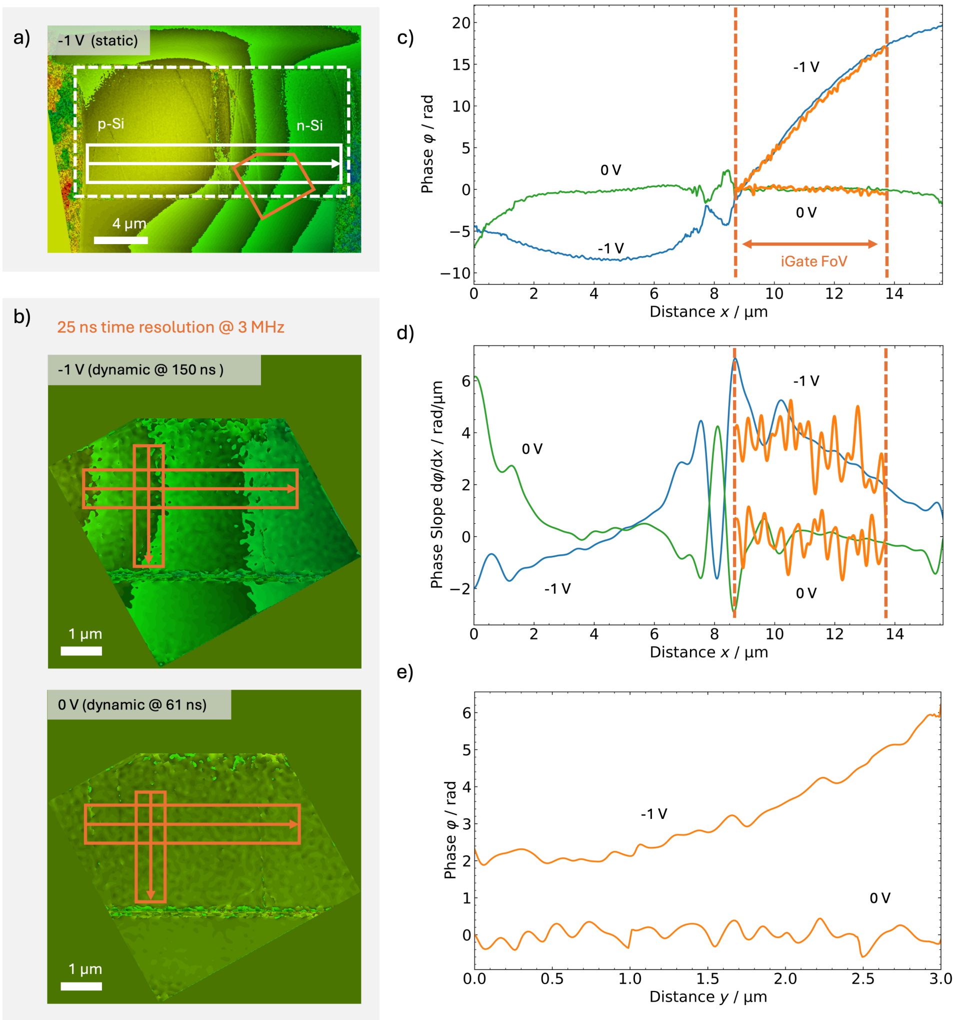

Figure 4. (**a**) Static phase reconstruction of the UG1A diode biased with −1 V, highlighting the space-charge region (SCR) between the p- and n-doped sides. The dashed white box outlines the area of the contacted TEM lamella; the orange polygon outlines the FoV for the time-resolved measurements. (**b**) Reconstructed dynamic phases, acquired with a time resolution of $\tau = 25\,\text{ns}$ at a repetition rate of $f = 3\,\text{MHz}$, showing the phase distribution for different switching states (−1 V at $t = 150\,\text{ns}$ and 0 V at $t = 61\,\text{ns}$) of the diode. The regions marked by orange lines indicate the areas used for the phase profiles in x- and y-directions. (**c**) Phase profiles at different biases (−1 V and 0 V) with orange dashed lines indicating the spatial range for time-resolved measurements (small FoV), (**d**) plot of the phase slopes along the x-axis, and (**e**) phase profiles along the y-axis for −1 V and 0 V.

Here, Figure 4c shows the phase profiles for the reverse-biased and unbiased conditions obtained from static measurements with a large field of view, along with the dynamic phase profiles from time-resolved measurements using iGate, superimposed in orange. It can be seen that the dynamic phases, which constitute an extract of the static phases, are in excellent agreement with these. However, it should be noted that the dynamic phases are inherently noisier than their static counterpart due to the limited signal-to-noise ratio (i.e., reduced contrast) imposed not only by iGate but also by the use of different detectors (K2 vs. US1000) and varying acceleration voltages (300 kV vs. 200 kV). Since, according to Equation (4), the derivative of the phase (phase slope) is proportional to the projected electric field, examining the derivative of the phase profiles is a common approach to evaluate operando EH. In this context, Figure 4d shows the derivative of the phase profiles $d\varphi/dx$ for both the static and time-resolved measurements. Since the dynamic phases are inherently noisier, this has a direct effect on the calculation of the phase slopes, for which reason the phase profiles first have to be smoothed using a Gaussian blur (here, $\sigma \approx 0.2\,\mu\text{m}$). This smoothing is in turn associated with an unavoidable loss of spatial information. It is noticeable that, despite this smoothing, the phase derivative profiles from the time-resolved measurements still exhibit a considerable degree of noise, which is why the evaluation of the phases slopes is not pursued further in this study.

Furthermore, the phase profiles in the y-direction outwards from the center of the diode towards its edge can likewise be examined in the time-resolved measurements (Figure 4e). This behavior is also evident in the static case, but it is absent in the simulations. Here, it is evident that no noticeable change in the phase course can be observed for the unbiased condition. For the reverse-biased condition, however, a steady increase towards the edge of the diode can be seen, which may indicate a possible implantation of Ga-ions. For these reasons, the temporal phase progression is analyzed in different regions of the diode (I–IV), shown hereafter in the dynamic phase image in Figure 5a.

Regions I and III (red and orange, respectively) are located near the center of the SCR, with region III close to the edge of the sample. Regions II and IV (blue and green, respectively), on the other hand, are located near the n-doped region of the diode, with region IV likewise close to the edge of the sample. Since the center of the SCR represents the zero phase, the phase courses increase according to the phase profiles in Figure 4c with greater distance from it. For improved comparability between the different investigated regions, the respective profiles of temporal phase progression are normalized (i.e., divided by their maximum value).

In Figure 5b, the temporal phase progression over the switching cycle of $T = 333.3\,\text{ns}$ (shown for an improved visualization as two repeated cycles from $t = 0\,\text{ns}$ to $t = 666.6\,\text{ns}$) in these four regions (I–IV), highlight the localized dynamics as the device switches between unbiased and reverse-biased states. Here, it should be noted that, at these low voltages (small signal condition), the diode under investigation behaves similarly to a very small capacitance. The current variation due to the small signal potential is therefore primarily governed by the junction capacitance. The rise times into the reverse-biased condition (first gray-shaded area, beginning around 100 ns) are similar for all regions, indicating a uniform response to the electric field buildup within the SCR. This synchronous phase rise across regions reflects the efficient establishment of reverse bias, quickly extending the SCR and influencing each region comparably. However, distinct differences emerge during the decay back to the unbiased state (second gray-shaded area, beginning around 265 ns). Regions I and II exhibit longer decay times, as represented by the broader gray-shaded area, while regions III and IV, near the sample edge, show shorter decay times, with narrower shaded areas.

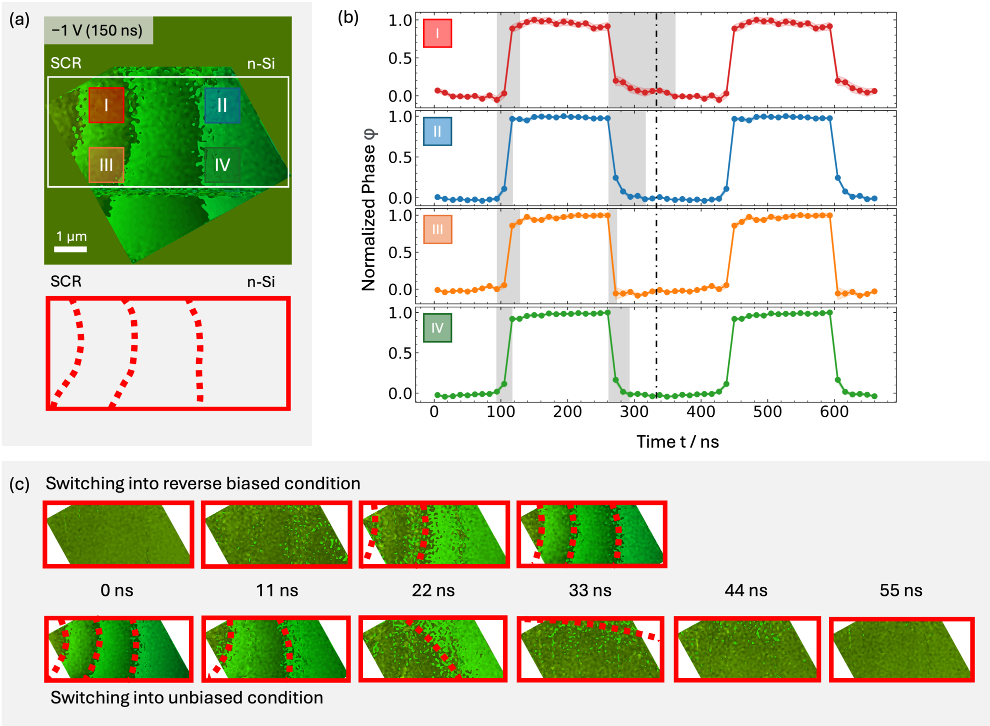

Figure 5. (**a**) Dynamic phase frame of the UG1A diode at −1 V bias (150 ns), depicting the SCR and its extension into the n-doped region, with the subregions (I–IV) marked for the analysis of the temporal phase progression (in (**b**)). The lower panel schematically illustrates the position of the equi-phase lines. (**b**) Normalized phase values over time, averaged in each subregion (I–IV) during diode switching, showing localized phase modulations corresponding to bias changes. The gray-shaded areas indicate the location-dependent transitions captured by iGate. For improved visibility, the period of $T = 333.3$ ns is repeated ($f = 3$ MHz). (**c**) Sequential phase frames of the switching behavior into and out of reverse-bias condition, demonstrating the temporal evolution of the equi-phase lines (red dashed) within the SCR.

To understand the variation in decay behavior, we need to take a closer look at the material characteristics and the sample preparation. As mentioned earlier, Ga-ions were applied during FIB preparation. When implanted into silicon, Ga can act as an acceptor and locally influence the properties of the diode. Regions I and II, deeper in the sample and less affected by Ga-implantation, may have longer decay times due to the more stable field retention within the SCR, where the electric field does not dissipate as rapidly. In contrast, regions III and IV, closer to the sample edge and with more Ga, may experience a quicker relaxation due to potential modifications in local charge dynamics. This is likely due to local modifications in charge dynamics, where Ga-related free charges near the edge could create pathways for quicker charge recombination. This disparity in decay times provides insight into how sample preparation artifacts and spatial location within the diode affect the relaxation dynamics, showcasing the complex interplay between intrinsic and extrinsic factors in the device's switching response.

The above-described behavior is also to some extent directly reflected in the phase frames. As a dynamic imaging method, iGate inherently enables direct observation and intuitive access to physical effects of the sample. The bottom panel of Figure 5a schematically depicts the equi-phase lines of the selected phase frame in the top panel as red dotted lines. The temporal progression of the individual phase frames for the switching processes into reverse-biased condition and back into unbiased condition are shown in Figure 5c. These originate from the time-resolved holograms with a time resolution of $\tau = 25$ ns at a sampling resolution of $\Delta t = 11.1\,\mathrm{ns}$. For the switching processes, the frame of the process start (i.e., start of the gray-shaded area in the plots in Figure 5b) was defined as the zero point in time.

Switching into reverse-biased condition is captured within four phase frames, from which a transition time of approx. 33 ns can be inferred. During this switching process, the equi-phase lines appear to move in from n-doped side in a fairly parallel manner. Switching back into unbiased condition, on the other hand, is captured within six phase frames, yielding a transition time of approx. 55 ns. Here, the parallel equi-phase lines show a counterclockwise twisting motion while moving back towards the n-doped side. This behavior is particularly consistent with the phase progressions from regions I and III. On the one hand, this suggests a slower decay process in the projected potential distribution, likely due to an extended transition time driven by diffusion. On the other hand, this decay process appears to be significantly accelerated at the sample's edge, manifesting itself in a twisting motion caused by recombination and/or conduction, attributed to the accumulation of charges from Ga-ion implantation in that region.

For an even better visualization, Video S1 shows an interpolated (i.e., bilinear interpolation with a factor of 10, correlating to the lines in the plots in Figure 5b) set of phase frames for the entire sampled period T. In this video, the counterclockwise twisting motion during the switching back into unbiased condition can be observed particularly well. Analogous to the previous observation, the time resolution of $\tau = 25\,\mathrm{ns}$ is not sufficient to adequately sample the mainly drift-driven switching process into reverse-biased condition. The absence of twisting motion here is not an indication of the non-existence of any recombination centers or an additional conduction channel in the edge region of the sample, but it is a direct confirmation of the different switching times of the various processes, which in turn is consistent with the electrical characterization in the supplement to [53].

4. Conclusions and Outlook

In this work, the application of a dynamic imaging of localized projected potentials of a contacted TEM lamella FIB, prepared out of a silicon diode in operando condition, was demonstrated using time-resolved electron holography. Here, the diode was operated between unbiased condition (i.e., $U_ext = 0\,\mathrm{V}$) and reverse-biased condition (i.e., $U_ext = -1\,\mathrm{V}$) at a repetition rate of $f = 3\,\mathrm{MHz}$, limited by the bandwidth of the signal generator used. This periodic process was sampled by interference gating with a time resolution of $\tau = 25\,\mathrm{ns}$ at a sampling rate of $\Delta t = 11.1\,\mathrm{ns}$, resulting in dynamic phase frames of the process with a spatial resolution of approx. 30 nm. These frames reflect the dynamics of the projected potential distribution in an area (field-of-view of approx. $5.3\,\mu\mathrm{m} \times 5.3\,\mu\mathrm{m}$) partially covering the space-charge region of the sample, in which the well-known diode properties are qualitatively preserved in the core of the lamella, while the effect of preparation-related ion implantation could be detected close to the edge of the lamella.

Equilibrium conditions serving as a reference were established through static biasing experiments, conducted with a larger field-of-view covering the entire sample (approx. $23.4\,\mu\mathrm{m} \times 24.6\,\mu\mathrm{m}$). The experimentally observed phase distributions in both static and dynamic measurements reflect the combined influences of reference wave perturbation, stray fields, and the intrinsic potential distribution within the space-charge region of the lamella. These contributions could be consistently modeled using a recently developed diffusion equation approach [55], enabling a qualitative understanding of the localized effects revealed in the experimental phase data. By comparing two phase frames from the dynamic measurements, representing the static reverse-biased and unbiased conditions, a correspondence between dynamic measurements with a limited field-of-view and static measurements with a larger field-of-view was established. This comparison allowed for the definition of two reference points, providing a framework for interpreting the phase progressions observed during the periodic switching processes.

During these switching processes, different dynamical behaviors, depending on the location within the space-charge region and with respect to the edge of the lamella, were observed. In the central area of the lamella, excellent agreement with the expected diode behavior was observed within the space-charge region as well as in the n-doped region. At the edge of the lamella, however, additional effects occurred, which can be attributed to additional conduction channels and recombination centers caused by preparation-dependent ion implantation. These effects can also be observed directly in the phase frames themselves, where a counterclockwise twisting motion of the equi-phase lines during the switching into unbiased condition reveals an increasing switching dynamic towards the edge of the lamella. By this, a new approach to the intuitive understanding of the ultrafast dynamics of projected potential distributions in such devices during switching processes is created, which, in its most visually appealing form, the phase video, highlights interference gating as a powerful tool in the operando investigation of switching electronic devices.

Since significantly higher spatial resolutions can easily be achieved in electron holography and the limited time resolution has so far only been due to technical limitations, a progression of the process into the nanoworld and thus the dynamic imaging of switching nano-devices seems logical. However, there are still hurdles to be overcome. The primary challenges to advancing this method can be assigned to the following key areas.

First, sample preparation poses significant difficulties, as the targeted and reproducible preparation of reliably switching nanostructures is essential. Parasitic currents on the surfaces due to redeposition, amorphized surfaces, and ion implantation introduce electrically unpredictable behavior, while the large distance between free-standing electrodes for contacting further complicates the process. Target-oriented solutions include the development of specialized carrier chips with significantly reduced electrode distances in vacuum conditions, coupled with highly adapted FIB-preparation routines to mitigate these effects, while reducing the overall preparation time.

Second, the perturbation of the reference wave by electric stray fields presents a substantial obstacle, significantly complicating the interpretability of reconstructed phases. Minimizing this modulation as far as possible is imperative. Particularly for operando investigations of electronic structures, the use of a "reference window" [57] has emerged as a promising approach to address this issue effectively.

Third, the projection problem, inherent to the projective nature of electron holography, must be addressed. Transmission electron microscopy is intrinsically sensitive to stray fields along the projection direction, which cannot be eliminated without substantial modifications to the sample. In operando investigations, this necessitates a strategy for incorporating these effects into the analysis. Consequently, simulations of the real three-dimensional sample geometry become indispensable for achieving a quantitative understanding of the experimental results.

Lastly, temporal resolution presents another critical challenge. With nanostructures expected to exhibit faster switching times, the achievable temporal resolution of the measurement method must likewise be improved. While instrumental advancements are necessary, modifying the gating signal offers an additional avenue for enhancement. For instance, recent studies have demonstrated that the temporal resolution in the same experimental setup could be improved to 1 ns [58] utilizing a square-wave-based gating signal, underscoring the feasibility of further refinement in this direction and bringing temporal resolutions in the picosecond range within a reachable distance.

This work establishes interference gating as a transformative approach for dynamic operando investigations of nanoscale electronic devices, bridging the gap between temporal and spatial resolution. By unlocking ultrafast imaging capabilities within conventional electron microscopy setups, iGate provides an intuitive and direct pathway to understanding high-speed processes at the nanoscale. As advancements in instrumentation and sample preparation further enhance this method, it holds the potential to redefine the boundaries of time-resolved microscopy, driving innovation in semiconductor research and beyond.

Supplementary Materials: The following supporting information can be downloaded at: https://www.mdpi.com/article/10.3390/electronics14010199/s1, Video S1: Dynamic phase evolution of the UG1A diode captured at 11 ns intervals during high-speed switching at 3 MHz.

Author Contributions: Conceptualization, T.W., H.Ç., S.G., I.H. and M.L.; methodology, T.W., H.Ç., S.G., I.H. and M.L.; software, T.W., H.Ç. and S.G.; validation, T.W., H.Ç., S.G., I.H., N.O. and F.H.; formal analysis, T.W., H.Ç., S.G., N.O., C.T.K. and F.H.; investigation, T.W., H.Ç., S.G., P.-H.L. and I.H.; resources, T.W., M.L., D.B., P.-H.L. and R.E.D.-B.; data curation, T.W., H.Ç., S.G., D.B., P.-H.L. and I.H.; writing—original draft preparation, T.W., H.Ç., S.G., D.B., P.-H.L., I.H., N.O., M.L., R.E.D.-B., C.T.K. and F.H.; writing—review and editing, T.W., H.Ç., S.G., D.B., P.-H.L., I.H., N.O., M.L., R.E.D.-B., C.T.K. and F.H.; visualization, T.W., H.Ç., S.G. and N.O.; supervision, T.W., H.Ç., M.L., C.T.K., P.-H.L., R.E.D.-B. and F.H.; project administration, T.W., H.Ç. and F.H. All authors have read and agreed to the published version of the manuscript.

Funding: This research received no external funding.

Data Availability Statement: Dataset available on request from the authors.

Acknowledgments: We thank the Technische Universität Berlin, Humboldt-Universität zu Berlin, and the Zentraleinrichtung Elektronenmikroskopie (ZELMI) in the context of the Alliance Center Electron Microscopy (ACEM) for support in acquisition (and analysis) of the data. The ACEM is funded under the Excellence Strategy of the Federal Government and the Länder by the Berlin University Alliance (BUA).

Conflicts of Interest: The authors declare no conflicts of interest.

Abbreviations

The following abbreviations are used in this manuscript:

iGate	Interference Gating
TEM	Transmission Electron Microscope
EH	Electron Holography
LM	Light Microscopy
SEM	Scanning Electron Microscopy
SIM	Scanning Ion Microscopy
FIB	Focused Ion Beam
Obj	Object Wave
Ref	Reference Wave
RF	Radio Frequency
FT	Fourier Transform
CB	Centerband
SB	Sideband
PRW	Perturbed Reference Wave
SIMP	Simple and Intuitive Model for Potentials
SCR	Space-Charge Region

References

1. Moore, G.E. Cramming more components onto integrated circuits. *Electronics* **1965**, *38*, 114–117. [CrossRef]
2. Alferov, Z.I. The history and future of semiconductor heterostructures. *Semiconductors* **1998**, *32*, 1–14. [CrossRef]
3. Flamm, K. Moore's law and the economics of semiconductor price trends. *Int. J. Technol. Policy Manag.* **2003**, *3*, 127–141. [CrossRef]
4. Jenkins, T. A brief history of ... semiconductors. *Phys. Educ.* **2005**, *40*, 430–439. [CrossRef]
5. Łukasiak, L.; Jakubowski, A. History of Semiconductors. *J. Telecommun. Inf. Technol.* **2010**, *2010*, 3–9. [CrossRef]
6. Mack, C.A. Fifty Years of Moore's Law. *IEEE Trans. Semicond. Manuf.* **2011**, *24*, 202–207. [CrossRef]
7. Klein, D. The History of Semiconductor Memory. *IEEE Solid-State Circuits Mag.* **2016**, *8*, 16–22. [CrossRef]
8. Leiserson, C.E.; Thompson, N.C.; Emer, J.S.; Kuszmaul, B.C.; Lampson, B.W.; Sanchez, D.; Schardl, T.B. There's plenty of room at the Top: What will drive computer performance after Moore's law? *Science* **2020**, *368*, eaam9744. [CrossRef]
9. IEEE. *The International Roadmap for Devices and Systems (IRDS) 2021 Edition*; IEEE: Piscataway, NJ, USA, 2021.
10. Vaughan, O. Two nanometre CMOS technology. *Nat. Electron.* **2024**, *7*, 1063–1063. [CrossRef]
11. Achoyan, A.S.; Yesayan, A.E.; Kazaryan, E.M.; Petrosyan, S.G. Two-dimensional p-n junction under equilibrium conditions. *Semiconductors* **2002**, *36*, 903–907. [CrossRef]
12. Blanco-Filgueira, B.; Martinez, P.L.; Aranda, J.B.R.; Hauer, J. Analytical Model for Crosstalk in p-n well Photodiodes. *IEEE Trans. Electron Devices* **2015**, *62*, 580–586. [CrossRef]
13. Ilatikhameneh, H.; Ameen, T.; Chen, F.; Sahasrabudhe, H.; Klimeck, G.; Rahman, R. Impact of Dimensionality on PN Junctions. *arXiv* **2016**, arXiv:1611.08784.
14. Ike Onyia, A.; Ifeanyi Ikeri, H.; Iheanyichukwu Chima, A. Surface and Quantum Effects in Nanosized Semiconductor. *Am. J. Nano Res. Appl.* **2020**, *8*, 35. [CrossRef]
15. Bank, R.E.; Bulirsch, R.; Merten, K. (Eds.) Mathematical Modelling and Simulation of Electrical Circuits and Semiconductor Devices. In *International Series of Numerical Mathematics*; Birkhäuser Verlag: Basel, Switzerland, 1990; Volume 93. [CrossRef]
16. Wachutka, G.; Schrag, G. (Eds.) *Simulation of Semiconductor Processes and Devices*; Springer: Vienna, Austria, 2004; Volume 10. [CrossRef]
17. Birner, S.; Hackenbuchner, S.; Sabathil, M.; Zandler, G.; Majewski, J.; Andlauer, T.; Zibold, T.; Morschl, R.; Trellakis, A.; Vogl, P. Modeling of Semiconductor Nanostructures with nextnano^3. *Acta Phys. Pol. A* **2006**, *110*, 111–124. [CrossRef]
18. Trellakis, A.; Zibold, T.; Andlauer, T.; Birner, S.; Smith, R.K.; Morschl, R.; Vogl, P. The 3D nanometer device project *Nextnano*: Concepts, Methods, Results.*J. Comput. Electron.* **2006**, *5*, 285–289. [CrossRef]
19. Birner, S.; Zibold, T.; Andlauer, T.; Kubis, T.; Sabathil, M.; Trellakis, A.; Vogl, P. nextnano: General Purpose 3D Simulations. *IEEE Trans. Electron Devices* **2007**, *54*, 2137–2142. [CrossRef]
20. McGilp, J.F. Optical characterisation of semiconductor surfaces and interfaces. *Prog. Surf. Sci.* **1995**, *49*, 1–106. [CrossRef]
21. Shah, J. *Ultrafast Spectroscopy of Semiconductors and Semiconductor Nanostructures*, 2nd ed.; Springer Science & Business Media: Berlin/Heidelberg, Germany, 2013.
22. Gutiérrez-D, E.A. *Nano-Scaled Semiconductor Devices—Physics, Modelling, Characterisation, and Societal Impact*, 1st ed.; Institution of Engineering and Technology: London, UK, 2016.
23. Kneissl, M.; Knorr, A.; Reitzenstein, S.; Hoffmann, A. *Semiconductor Nanophotonics—Materials, Models, and Devices*, 1st ed.; Springer Science & Business Media: Berlin/Heidelberg, Germany, 2020.
24. Hawkes, P.W.; Spence, J.C. *Springer Handbook of Microscopy*, 1st ed.; Springer Science & Business Media: Berlin/Heidelberg, Germany, 2019.
25. Möllenstedt, G.; Wahl, H. Elektronenholographie und Rekonstruktion mit Laserlicht. *Die Naturwissenschaften* **1968**, *55*, 340–341. [CrossRef]
26. Matteucci, G.; Missiroli, G.F.; Chen, J.W.; Pozzi, G. Mapping of microelectric and magnetic fields with double-exposure electron holography. *Appl. Phys. Lett.* **1988**, *52*, 176–178. [CrossRef]
27. Tonomura, A. *Electron Holography*, 2nd ed.; Springer Science & Business Media: Berlin/Heidelberg, Germany, 1999.
28. Rau, W.D.; Schwander, P.; Baumann, F.H.; Höpner, W.; Ourmazd, A. Two-Dimensional Mapping of the Electrostatic Potential in Transistors by Electron Holography. *Phys. Rev. Lett.* **1999**, *82*, 2614–2617. [CrossRef]
29. McCartney, M.R.; Smith, D.J.; Hull, R.; Bean, J.C.; Voelkl, E.; Frost, B. Direct observation of potential distribution across Si/Si p-n junctions using off-axis electron holography. *Appl. Phys. Lett.* **1994**, *65*, 2603–2605. [CrossRef]
30. Twitchett, A.C.; Dunin-Borkowski, R.E.; Midgley, P.A. Quantitative Electron Holography of Biased Semiconductor Devices. *Phys. Rev. Lett.* **2002**, *88*, 238302. [CrossRef] [PubMed]
31. He, K.; Cho, J.H.; Jung, Y.; Tom Picraux, S.; Cumings, J. Silicon nanowires: Electron holography studies of doped p–n junctions and biased Schottky barriers. *Nanotechnology* **2013**, *24*, 115703. [CrossRef] [PubMed]

32. Gatel, C.; Serra, R.; Gruel, K.; Masseboeuf, A.; Chapuis, L.; Cours, R.; Zhang, L.; Warot-Fonrose, B.; Hÿtch, M. Extended Charge Layers in Metal-Oxide-Semiconductor Nanocapacitors Revealed by Operando Electron Holography. *Phys. Rev. Lett.* **2022**, *129*, 137701. [CrossRef] [PubMed]
33. Zhang, L.; Raza, M.H.; Wu, R.; Gruel, K.; Dubourdieu, C.; Hÿtch, M.; Gatel, C. Quantification of Interfacial Charges in Multilayered Nanocapacitors by Operando Electron Holography. *Adv. Mater.* **2024**, 2413691. [CrossRef]
34. Cooper, D.; Bruas, L.; Bryan, M.; Boureau, V. Measuring electrical properties in semiconductor devices by pixelated STEM and off-axis electron holography (or convergent beams vs. plane waves). *Micron* **2024**, *179*, 103594. [CrossRef]
35. Feist, A.; Echternkamp, K.E.; Schauss, J.; Yalunin, S.V.; Schäfer, S.; Ropers, C. Quantum coherent optical phase modulation in an ultrafast transmission electron microscope. *Nature* **2015**, *521*, 200–203. [CrossRef]
36. Houdellier, F.; Caruso, G.; Weber, S.; Hÿtch, M.; Gatel, C.; Arbouet, A. Optimization of off-axis electron holography performed with femtosecond electron pulses. *Ultramicroscopy* **2019**, *202*, 26–32. [CrossRef]
37. Niermann, T.; Lehmann, M. Averaging scheme for atomic resolution off-axis electron holograms. *Micron* **2014**, *63*, 28–34. [CrossRef]
38. Wagner, T.; Niermann, T.; Urban, F.; Lehmann, M. Nanosecond electron holography by interference gating. *Ultramicroscopy* **2019**, *206*, 112824. [CrossRef]
39. Vishay Intertechnology. *UG1A, UG1B, UG1C, UG1D Miniature Ultrafast Plastic Rectifier (Datasheet)*; Vishay Intertechnology: Malvern, PA, USA, 2018.
40. Tonomura, A. Applications of electron holography. *Rev. Mod. Phys.* **1987**, *59*, 639–669. [CrossRef]
41. Cowley, J. Twenty forms of electron holography. *Ultramicroscopy* **1992**, *41*, 335–348. [CrossRef]
42. Völkl, E.; Joy, D.C. *Introduction to Electron Holography*, 1st ed.; Springer Science & Business Media: Berlin/Heidelberg, Germany, 1999.
43. Möllenstedt, G.; Düker, H. Beobachtungen und Messungen an Biprisma-Interferenzen mit Elektronenwellen. *Z. Für Phys.* **1956**, *145*, 377–397. [CrossRef]
44. Matteucci, G.; Missiroli, G.; Nichelatti, E.; Migliori, A.; Vanzi, M.; Pozzi, G. Electron holography of long-range electric and magnetic fields. *J. Appl. Phys.* **1991**, *69*, 1835–1842. [CrossRef]
45. Matteucci, G.; Missiroli, G.; Muccini, M.; Pozzi, G. Electron holography in the study of the electrostatic fields: The case of charged microtips. *Ultramicroscopy* **1992**, *45*, 77–83. [CrossRef]
46. Pozzi, G., Electron holography of long-range electromagnetic fields: A tutorial. In *Microscopy, Spectroscopy, Holography and Crystallography with Electrons*; Elsevier: Amsterdam, The Netherlands, 2002; pp. 207–223. [CrossRef]
47. Michelson, A.A. Visibility of Interference-Fringes in the Focus of a Telescope. *Publ. Astron. Soc. Pac.* **1891**, *3*, 217–220. [CrossRef]
48. Boothroyd, C.; Kovács, A.; Tillmann, K. FEI Titan G2 60-300 HOLO. *J. Large-Scale Res. Facil. JLSRF* **2016**, *2*, A44. [CrossRef]
49. Völkl, E.; Allard, L.F.; Frost, B. A software package for the processing and reconstruction of electron holograms. *J. Microsc.* **1995**, *180*, 39–50. [CrossRef]
50. Gatan, I. DigitalMicrograph. 2024. Available online: https://www.gatan.com/products/tem-analysis/gatan-microscopy-suite-software (accessed on 2 January 2025).
51. Genz, F.; Niermann, T.; Buijsse, B.; Freitag, B.; Lehmann, M. Advanced double-biprism holography with atomic resolution. *Ultramicroscopy* **2014**, *147*, 33–43. [CrossRef]
52. Wagner, T. Interference Gating—A Novel Method for Time-Resolved Off-Axis Electron Holography. Ph.D. Thesis, Technische Universität Berlin, Berlin/Heidelberg, Germany, 2022.
53. Wagner, T.; Çelik, H.; Lehmann, M.; Berger, D.; Häusler, I. Imaging localized variable capacitance during switching processes in silicon diodes by time-resolved electron holography. *Phys. Rev. B* **2024**, *109*, 085310. [CrossRef]
54. Zhang, H. What limits the application of TEM in the semiconductor industry? *Thin Solid Film* **1998**, *320*, 77–85. [CrossRef]
55. Çelik, H.; Fuchs, R.; Gaebel, S.; Günther, C.M.; Lehmann, M.; Wagner, T. A simple and intuitive model for long-range 3D potential distributions of in-operando TEM-samples: Comparison with electron holographic tomography. *Ultramicroscopy* **2024**, *267*, 114057. [CrossRef] [PubMed]
56. Sze, S.M.; Li, Y.; Ng, K.K. *Physics of Semiconductor Devices*, 4th ed.; John Wiley & Sons: Hoboken, NJ, USA, 2021.
57. Wagner, T.; Kraft, R.; Nowak, F.; Berger, D.; Günther, C.M.; Çelik, H.; Koch, C.T.; Lehmann, M. The reference window for reduced perturbation of the reference wave in electrical biasing off-axis electron holography. *Ultramicroscopy* **2024**, *267*, 114060. [CrossRef] [PubMed]
58. Gaebel, S.; Çelik, H.; Berger, D.; Koch, C.T.; Lehmann, M.; Wagner, T. Approaching One Nanosecond Temporal Resolution with Square-Wave-Based Control Signals for Interference Gating. *Ultramicroscopy* 2024, *Under Review*.